ACTIVE 6 DoF FORCE/TORQUE CONTROL BASED ON DYNAMIC JACOBIAN FOR FREE-FLOATING SPACE MANIPULATOR

Filip DYBA[1,2], Tomasz RYBUS[1], Mateusz WOJTUNIK[1],
Fatina Liliana BASMADJI[1]

[1] Centrum Badań Kosmicznych Polskiej Akademii Nauk (CBK PAN),
Warsaw, Poland
[2] Wroclaw University of Science and Technology, Wroclaw, Poland

e-mails: filip.dyba@pwr.edu.pl, trybus@cbk.waw.pl, mwojtunik@cbk.waw.pl,
fbasmadji@cbk.waw.pl

ABSTRACT. In-orbit capture of a non-cooperative satellite will be a major challenge in the proposed servicing and active debris removal missions. The contact forces between the manipulator end-effector and the elements of the target object will occur in the grasping phase. In this paper, an active 6 Degrees of Freedom (DoF) force/torque control method for manipulator mounted on a free-floating servicing satellite is proposed. The main aim of the presented method is to balance the relation between end-effector position and force along each direction in the Cartesian space. The control law is based on the Dynamic Jacobian, which takes into account the influence of the manipulator motion on the state of the servicing satellite. The proposed approach is validated in numerical simulations with a simplified model of contact. Comparison with the classical Cartesian control shows that the active 6 DoF force/torque control method allows to obtain better positioning accuracy of the end-effector and lower control torques in manipulator joints in the presence of external forces.

Keywords: active force/torque control, free-floating manipulator, Dynamic Jacobian, capture manoeuvre, in-orbit servicing

1. INTRODUCTION

Small, unmanned servicing satellites will be used to conduct in-orbit servicing and active debris removal missions (Luu and Hastings, 2021). Capture of the target object will be a major challenge of the proposed missions (Fehse, 2014). One of the considered ways to perform the capture operation is to use a gripper mounted on a robotic manipulator (Shan et al., 2016; Henshaw et al., 2022). The contact forces between the gripper and the elements of the target object will occur in the grasping phase (Oleś et al., 2017). These forces can result in a very high load acting on the manipulator or they can cause the target object to drift away from the servicing satellite. Thus, managing the contact dynamics between the satellite-manipulator system and the target object is one of the fundamental capabilities required to enable servicing and active debris removal missions (Tasker and Henshaw, 2008).

Various approaches are proposed to control the manipulator during its interaction with the environment (Villani and De Schutter, 2016). The compliant control can be divided into two main categories: (i) the active compliant control and (ii) the passive compliant control. In the

active compliant control, the compliance is achieved entirely due to control, while in the passive compliant control, it is achieved entirely due to mechanics (Calanca et al., 2016). In the passive compliant control the contact with the environment is controlled using an element of elasticity like a soft interface to the environment, whereas the classical position control law is considered. The active compliant control is divided into direct force control and indirect force control. Direct force control includes hybrid force and position control proposed by Raibert and Craig (1981). In such an approach, the task space is decomposed into different sets and directions, where either motion or force is controlled. The indirect force control allows to regulate the dynamic interaction between the manipulator and its environment. As a consequence, the relationship between forces and motion is regulated. Such a method is very useful for in-orbit capture operations as it allows to minimise loads acting on the manipulator during positioning of the gripper.

Several studies are devoted to application of compliant control methods for the case of orbital capture operation. Liu et al. (2020a) proposed a position-based impedance control strategy based on mass-damping model that prevents the non-cooperative target object from moving away after contact with the end-effector. In the impedance control approach proposed by Nakanishi and Yoshida (2006), the end-effector of the manipulator is controlled like a spring-mass-damper system fixed at a given point in the inertial frame in spite of the reactive motion of the servicing satellite. In another approach, based on a hybrid control scheme with damping and attitude tracking controllers, only the kinematic information of the space robot is employed as the control feedback, which can be considered as an advantage over the classical impedance control (Liu et al., 2020b). Wu et al. (2017) proposed a combination of admittance control method with resolved motion rate control. This approach allows to reduce the relative velocity at the contact spots and increase the compliance of the manipulator during contact. Pérez et al. (2018) proposed a method for tuning an impedance control scheme to ensure post-impact velocity matching between the servicing satellite and the target object. Uyama et al. (2012) presented an open-loop impedance control law that allows to obtain the desired coefficient of restitution defined between the gripper and the grasping point on the free-floating target object. The proposed approach was validated in experiments performed on a planar air-bearing microgravity simulator. García et al. (2019) presented validation of impedance control in hardware-in-the-loop experiments performed on the platform-art facility. Palma et al. (2022) proposed control with mechanical impedance realised along a single axis for facilitating contact between the end-effector and the target object.

In this paper, we propose an active 6 Degrees of Freedom (DoF) force/torque closed-loop control method for manipulator mounted on a servicing satellite. In the case of no external forces and torques apart from those resulting from contact, such a system is referred to as free-floating (Wilde et al., 2018). The active 6 DoF force/torque algorithm is based on the admittance control with spring-mass-damper model. The contact force acting on the end-effector is taken into account. The main aim of the proposed method is to balance the relation between the end-effector position and force along each direction in the Cartesian space. The control law is based on the Dynamic Jacobian, which takes into account the influence of the manipulator motion on the state of the servicing satellite. In the control algorithm, it is assumed that the linear and angular momenta are conserved and equal to zero. However, in reality, the momenta change due to the external forces acting on the end-effector. The changes are treated as a disturbance. The proposed approach is an extension of the method developed for post-capture operations in the e.Deorbit mission (Basmadji et al., 2018). The active 6 DoF force/torque control is validated in numerical simulations with a simplified model of contact. In the considered scenario, the end-effector is controlled to approach the selected grasping

point on the Launch Adapter Ring (LAR) of a non-cooperative target satellite. The proposed method is compared with the classical Cartesian control (Rybus et al., 2017).

The paper is organised as follows. The dynamic model of the free-floating space manipulator is presented in Section 2. The proposed control method is described in Section 3. The results of numerical simulations are shown in Section 4. Section 5 contains discussion of the obtained results. The paper concludes with a short summary given in Section 6.

2. DYNAMICS OF FREE-FLOATING MANIPULATOR

The dynamic equations of motion of the satellite-manipulator system are based on the equations presented by Seweryn and Banaszkiewicz (2008) and Rybus et al. (2017). The schematic view of the system is shown in Figure 1. The scheme presents a manipulator (with n rotational joints) mounted on the free-floating base – a servicing satellite. The inertial frame of reference Π_{ine} is non-moving, non-rotating and fixed to an arbitrarily selected point in the Cartesian space. In the following notation, the frames of reference in which the vectors are expressed are given in the superscript. If the variables are expressed in the inertial frame, then the superscript is omitted for simplicity.
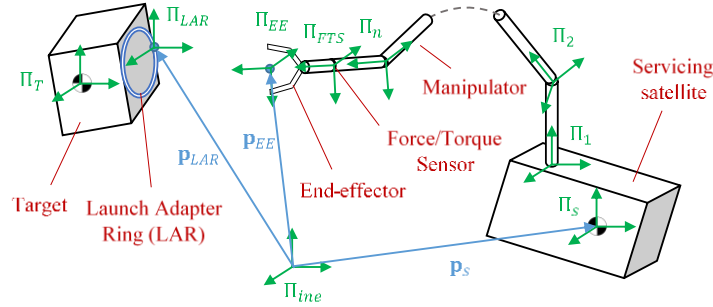

Figure 1. Schematic view of the satellite-manipulator system

The configuration of the system is described by $6+n$ generalised coordinates:

$$\mathbf{x}_p = [\mathbf{P}_s^T \quad \mathbf{q}^T]^T, \tag{1}$$

where $\mathbf{P}_s = [\mathbf{p}_s^T \quad \boldsymbol{\varphi}_s^T]^T$, $\mathbf{p}_s$ denotes the position vector of the servicing satellite centre of mass (CoM), $\boldsymbol{\varphi}_s$ denotes the vector of the servicing satellite orientation described by three Euler angles in ZYX convention, whereas $\mathbf{q}$ denotes the vector of manipulator joint angles.

The vector of generalised velocities of the satellite-manipulator system is defined as follows:

$$\mathbf{x}_v = \begin{bmatrix} \mathbf{V}_s^T & \dot{\mathbf{q}}^T \end{bmatrix}^T, \tag{2}$$

where $\mathbf{V}_s = [\mathbf{v}_s^T \quad \boldsymbol{\omega}_s^T]^T$, $\mathbf{v}_s$ denotes the linear velocity vector of the servicing satellite CoM, $\boldsymbol{\omega}_s = \mathbf{T}_{eul}\dot{\boldsymbol{\Theta}}_s$ denotes the angular velocity vector of the servicing satellite ($\mathbf{T}_{eul}$ is the transformation matrix that maps Euler angles derivatives into the angular body velocity), whereas $\dot{\mathbf{q}}$ denotes the vector of manipulator joint angular velocities.

The dynamics of the satellite-manipulator system is described by the equation

$$\begin{bmatrix} \mathbf{M}_s & \mathbf{M}_{sm} \\ \mathbf{M}_{sm}^T & \mathbf{M}_m \end{bmatrix} \dot{\mathbf{x}}_v + \begin{bmatrix} \mathbf{C}_s \\ \mathbf{C}_m \end{bmatrix} \mathbf{x}_v = \mathbf{Q}, \tag{3}$$

where $\mathbf{M}_s$ and $\mathbf{M}_m$ are mass matrices of the servicing satellite and the manipulator, respectively, $\mathbf{M}_{sm}$ is the mass matrix that couples the dynamics of the servicing satellite and the manipulator, $\mathbf{C}_s$ and $\mathbf{C}_m$ are Coriolis matrices of the servicing satellite and the

manipulator, respectively (each matrix is defined by Rybus et al., 2022), whereas $\mathbf{Q}$ denotes the vector of generalised forces given by the following equation:

$$\mathbf{Q} = [\mathbf{F}_s^T \quad \mathbf{u}^T]^T, \tag{4}$$

where $\mathbf{F}_s = [\mathbf{f}_s^T \quad \boldsymbol{\tau}_s^T]^T$, $\mathbf{f}_s$ denotes the vector of external forces acting on the servicing satellite CoM, $\boldsymbol{\tau}_s$ denotes the vector of external torques acting on the servicing satellite and $\mathbf{u}$ is the vector of control torques applied to the manipulator joints.

The linear and angular velocity of the manipulator end-effector is described by the following relation:

$$\mathbf{V}_{EE} = \mathbf{J}_s \mathbf{V}_s + \mathbf{J}_m \dot{\mathbf{q}}, \tag{5}$$

where $\mathbf{J}_s$ denotes the Jacobian of the servicing satellite and $\mathbf{J}_m$ is the standard fixed-base Jacobian of the manipulator.

In case of the manipulator operating in close proximity to the target object, the servicing satellite Attitude and Orbit Control System (AOCS) is considered to be turned off. In addition, the gravity gradient is neglected due to relatively small size of the manipulator (Cavenago, 2019). Therefore, the external forces and torques acting on the servicing satellite CoM are equal to zero: $\mathbf{F}_s = \mathbf{0}$. The system is then nonholonomic and has conserved linear and angular momenta (Ratajczak and Tchoń, 2020). The nonholonomic constraint of the system is written in the form

$$\mathbf{H}_2 \mathbf{V}_s + \mathbf{H}_3 \dot{\mathbf{q}} = \mathbf{0}, \tag{6}$$

where matrices $\mathbf{H}_2$ and $\mathbf{H}_3$ are defined by Rybus et al. (2022).

Solving (6) for linear and angular velocity of the servicing satellite and substituting into (5) yields

$$\mathbf{V}_{EE} = \mathbf{J}_{dyn} \dot{\mathbf{q}}, \tag{7}$$

where $\mathbf{J}_{dyn}$ is the Dynamic Jacobian of the manipulator described by Rybus et al. (2012) as follows:

$$\mathbf{J}_{dyn} = \mathbf{J}_m - \mathbf{J}_s \mathbf{H}_2^{-1} \mathbf{H}_3. \tag{8}$$

The Dynamic Jacobian of the manipulator takes the dynamics of the servicing satellite into account by assumption of zero momenta and angular momenta of the system and allows to map the manipulator joint velocities into the linear and angular velocities of the end-effector for the free-floating case. The Dynamic Jacobian presented in (8) is expressed in the Π_{ine} frame. However, by multiplying the Jacobian with proper rotation matrix, it can be expressed in any arbitrarily chosen frame of reference, for example, the Dynamic Jacobian can be expressed in Π_{EE} frame leading to mapping into end-effector velocities expressed in the Π_{EE} frame (such a matrix will be denoted as $\mathbf{J}_{dyn}^{(EE)}$).

3. ACTIVE 6 DoF FORCE/TORQUE CONTROL

The main aim of the active 6 DoF force/torque control is to balance the relation between end-effector position and force along each direction in the Cartesian space (Almeida et al., 2000). In the proposed approach, manipulator's interaction with its environment is taken into account. Hence, the manipulator motion and acting forces are taken into consideration simultaneously in one control task. The compliance of the external forces is entirely guaranteed by the control algorithm, and the influence of the mechanics does not need to be considered (Calanca et al., 2016). The '6 DoF' term in the method name refers to three

reaction forces and three reaction torques which act on the manipulator gripper. The presented method is applicable for the grasping phase, in which the end-effector is approaching LAR of the non-cooperative target satellite. The active 6 DoF force/torque control is based on the method proposed by Basmadji et al. (2018) for positioning an already captured target satellite during clamping operation in the e.Deorbit mission. A scheme of the control algorithm presented in this section is shown in Figure 2.
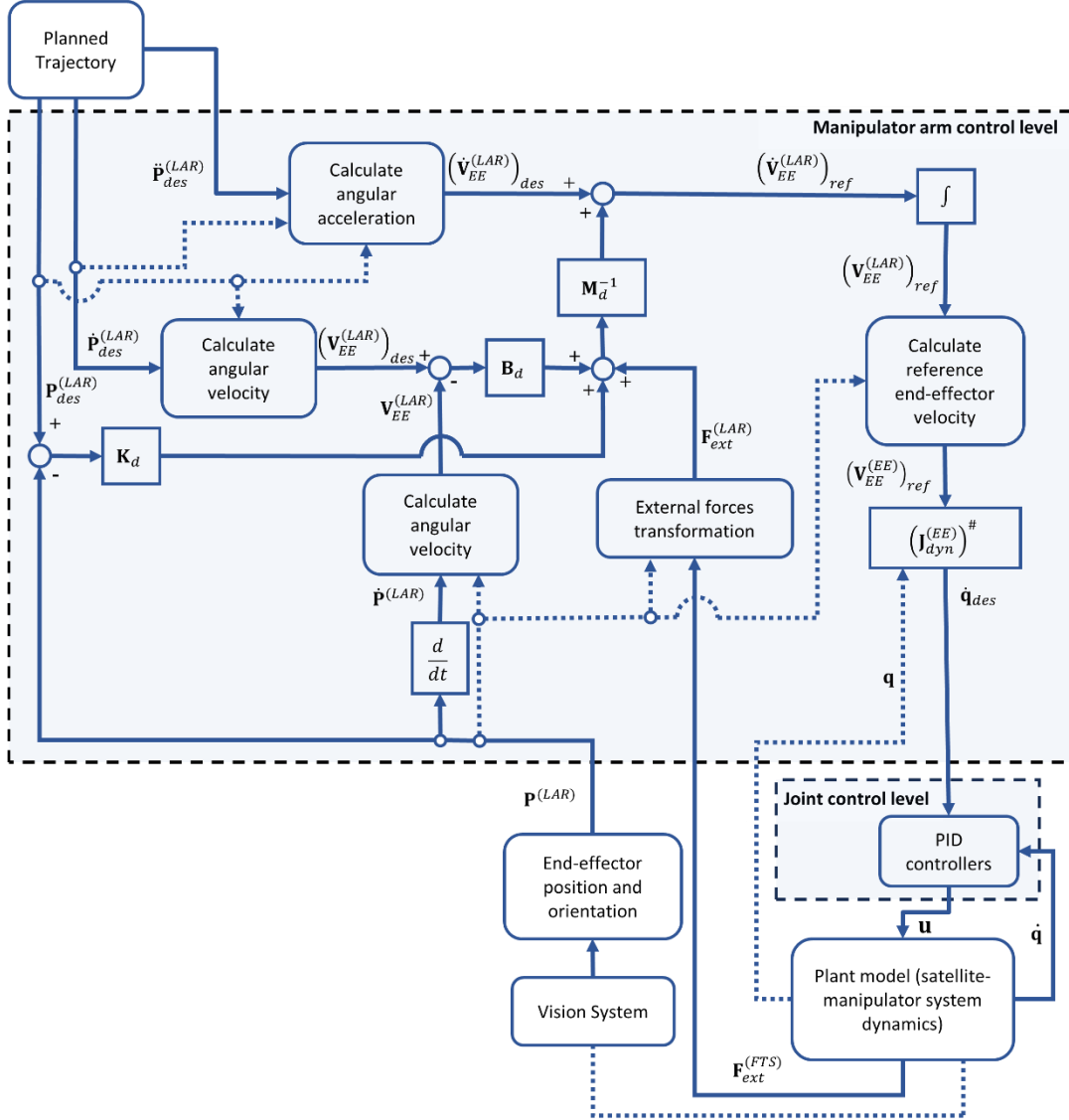

Figure 2. Scheme of the active 6 DoF force/torque control algorithm (solid lines – input/output signals, dotted lines – dependencies/values required for calculation)

It is worth noticing that the considered algorithm does not allow to follow the desired force trajectory, but it is a position control scheme with some adjustments to reduce the external forces acting on the gripper. In this approach, the manipulator is treated as a mechanical system with certain mass, stiffness and damping defined by gain matrices (Wang and Li, 2010). A system of such properties may be formulated as

$$\mathbf{M}_d \left(\dot{\mathbf{V}}_{EE}^{(LAR)} - \left(\dot{\mathbf{V}}_{EE}^{(LAR)} \right)_{des} \right) + \mathbf{B}_d \left(\mathbf{V}_{EE}^{(LAR)} - \left(\mathbf{V}_{EE}^{(LAR)} \right)_{des} \right) +$$
$$+ \mathbf{K}_d \left(\mathbf{P}_{EE}^{(LAR)} - \left(\mathbf{P}_{EE}^{(LAR)} \right)_{des} \right) = \mathbf{F}_{ext}^{(LAR)}, \tag{9}$$

where $\dot{\mathbf{V}}_{EE}^{(LAR)}$ is the vector containing the current linear and angular acceleration of the end-effector, $\mathbf{V}_{EE}^{(LAR)}$ is the vector of the current linear and angular velocity of the end-effector, $\mathbf{P}_{EE}^{(LAR)}$ is the vector of the current position and orientation of the end-effector, vectors with *des* in the subscript denote respective desired values, $\mathbf{M}_d$ is the positive-definite matrix representing the desired inertia, $\mathbf{B}_d$ is the positive-definite matrix representing the desired damping, $\mathbf{K}_d$ is the positive-definite matrix representing the desired stiffness and $\mathbf{F}_{ext}^{(LAR)}$ represents the external forces and torques acting on the end-effector. In the considered approach, all values are expressed with respect to the LAR reference frame, which is denoted with (LAR) in the superscript. Orientations considered in (9) are described by Euler angles in ZYX convention with respect to the LAR frame, $\boldsymbol{\varphi}_{EE}^{(LAR)}$. Hence, geometric angular velocity in the Cartesian space may be calculated as follows:

$$\boldsymbol{\omega}_{EE}^{(EE)} = \mathbf{T}_{eul}\dot{\boldsymbol{\varphi}}_{EE}^{(LAR)}. \tag{10}$$

To calculate Cartesian space angular accelerations, equation (10) needs to be differentiated:

$$\dot{\boldsymbol{\omega}}_{EE}^{(EE)} = \dot{\mathbf{T}}_{eul}\dot{\boldsymbol{\varphi}}_{EE}^{(LAR)} + \mathbf{T}_{eul}\ddot{\boldsymbol{\varphi}}_{EE}^{(LAR)}. \tag{11}$$

However, values in (10) and (11) are expressed in the end-effector body reference frame, so they have to be transformed to the LAR reference frame:

$$\boldsymbol{\omega}_{EE}^{(LAR)} = \mathbf{R}_{EE}^{LAR}\boldsymbol{\omega}_{EE}^{(EE)}, \tag{12}$$

$$\dot{\boldsymbol{\omega}}_{EE}^{(LAR)} = \dot{\mathbf{R}}_{EE}^{LAR}\boldsymbol{\omega}_{EE}^{(EE)} + \mathbf{R}_{EE}^{LAR}\dot{\boldsymbol{\omega}}_{EE}^{(EE)}, \tag{13}$$

where $\mathbf{R}_{EE}^{LAR}$ is the rotation matrix that converts angular velocities from the end-effector body reference frame to the LAR reference frame.

According to (9), the reference trajectory of the linear and angular accelerations may be defined as

$$\left(\dot{\mathbf{V}}_{EE}^{(LAR)}\right)_{ref} = \left(\dot{\mathbf{V}}_{EE}^{(LAR)}\right)_{des} + \mathbf{M}_d^{-1}\left(\mathbf{F}_{ext}^{(LAR)} + \mathbf{B}_d\left(\left(\mathbf{V}_{EE}^{(LAR)}\right)_{des} - \mathbf{V}_{EE}^{(LAR)}\right)\right) +$$
$$+\mathbf{M}_d^{-1}\,\mathbf{K}_d\left(\left(\mathbf{P}_{EE}^{(LAR)}\right)_{des} - \mathbf{P}_{EE}^{(LAR)}\right). \tag{14}$$

To formulate the control law, the reference linear and angular velocities of the end-effector expressed with respect to the body reference frame need to be calculated. Thus, equation (14) is integrated as follows:

$$\left(\mathbf{V}_{EE}^{(LAR)}\right)_{ref} = \int\left(\dot{\mathbf{V}}_{EE}^{(LAR)}\right)_{ref} dt + \left(\left(\mathbf{V}_{EE}^{(LAR)}\right)_{ref}\right)_0, \tag{15}$$

where subscript 0 denotes the initial condition. Furthermore, the reference velocities from (15) need to be transformed to the body reference frame:

$$\left(\mathbf{V}_{EE}^{(EE)}\right)_{ref} = \begin{bmatrix} \mathbf{R}_{LAR}^{EE} & \mathbf{0}_{3\times3} \\ \mathbf{0}_{3\times3} & \mathbf{R}_{LAR}^{EE} \end{bmatrix}\left(\mathbf{V}_{EE}^{(LAR)}\right)_{ref}. \tag{16}$$

Finally, the control law defining the desired joint angular velocities can be formulated as follows:

$$\dot{\mathbf{q}}_{des} = \left(\mathbf{J}_{dyn}^{(EE)}\right)^{\#}\left(\mathbf{V}_{EE}^{(EE)}\right)_{ref}, \tag{17}$$

where # denotes Moore–Penrose pseudoinverse of a matrix. Although the Dynamic Jacobian, defined with (8), assumes the conservation of the linear and angular momenta, the control law correctly compensates disturbances resulting from the external forces and torques acting on the end-effector. The forces and torques are included in the definition of the reference velocities (equations (14)–(16)).

External forces and torques are nominally measured in the force/torque sensor reference frame. The sensor is located between the seventh link of the manipulator and the end-effector. Thus, the measurement needs to be properly translated to Π_{EE} frame to describe the impact of external forces on the end-effector:

$$\mathbf{F}_{ext}^{(EE)} = \mathbf{F}_{ext}^{(FTS)} + \begin{bmatrix} \mathbf{0}_{3\times1} \\ \mathbf{p}_{EE}^{(FTS)} \otimes \mathbf{f}^{(FTS)} \end{bmatrix}, \tag{18}$$

where $\mathbf{p}_{EE}^{(FTS)}$ is the location of the end-effector with respect to the force/torque sensor frame and $\otimes$ denotes the cross product of vectors. Subsequently, values from (18) need to be transformed to the LAR frame according to the following equation:

$$\mathbf{F}_{ext}^{(LAR)} = \begin{bmatrix} \mathbf{R}_{EE}^{LAR} & \mathbf{0}_{3\times3} \\ \mathbf{0}_{3\times3} & \mathbf{R}_{EE}^{LAR} \end{bmatrix} \mathbf{F}_{ext}^{(EE)}. \tag{19}$$

4. RESULTS OF NUMERICAL SIMULATIONS

In the conducted simulations, a redundant manipulator is considered. Its Denavit–Hartenberg parameters are presented in Table 1. Table 2 presents i-th link mass and its CoM position defined with respect to Π_i (expressed in Π_i). Inertia properties of every link expressed with respect to its CoM in the local frame axes are shown in Table 3.

The manipulator is mounted on the servicing satellite. Position of the mounting point is defined in the satellite frame as $\mathbf{p}_{MP}^{(s)} = [0.2\,\text{m} \quad 0.2\,\text{m} \quad 0.2\,\text{m}]^T$. It is assumed that the chaser inertia matrix is equal to $\mathbf{I}_s = diag_{3\times3}[79\,\text{kg m}^2 \quad 79\,\text{kg m}^2 \quad 117\,\text{kg m}^2]$ and its mass is 500 kg.

Table 1. Denavit–Hartenberg parameters of the manipulator

Link i	q_i (rad)	λ_i (m)	L_i (m)	α_i (rad)
1	$q_1 + \pi/2$	0.4	0	$\pi/2$
2	$q_2 + \pi/2$	−0.35	0	$\pi/2$
3	q_3	−0.3	0.6	0
4	q_4	−0.35	0.35	0
5	q_5	−0.3	0	$-\pi/2$
6	$q_6 + \pi/2$	0.3	0	$\pi/2$
7	q_7	0.25	0	0
EE	0	0.175	0	0

Table 2. Link CoM positions and masses

Link	X (m)	Y (m)	Z (m)	Mass (kg)
1	0	0.3	0	15
2	0	−0.25	0	13
3	0.3	0	−0.2	18
4	0.25	0	−0.35	10
5	0	0.2	0	8.5
6	0	0.25	0	10.5
7	0	0	0.1	5
EE	0	0	0.1	7

Table 3. Link inertia properties

Link	I_{xx} (kg m^2)	I_{yy} (kg m^2)	I_{zz} (kg m^2)	I_{xy} (kg m^2)	I_{xz} (kg m^2)	I_{yz} (kg m^2)
1	0.2	0.15	0.1	0	0	0
2	0.2	0.12	0.12	0	0	0
3	0.3	1	1	0	0.2	0
4	0.08	0.45	0.4	0	0.1	0
5	0.6	0.55	0.35	0	0	0
6	0.75	0.4	0.7	0	0	0
7	0.3	0.3	0.3	0	0	0
EE	0.09	0.05	0.12	0	0	0

To validate the control system, the following simulation scenario is assumed. The manoeuvre of grasping LAR is considered. The initial configuration of the manipulator is $\mathbf{q}_{init} = [q_1 \quad q_2 \quad q_3 \quad q_4 \quad q_5 \quad q_6 \quad q_7]^T$, where $q_1 = 2.196$ rad, $q_2 = -2.386$ rad, $q_3 = -2.011$ rad, $q_4 = 2.595$ rad, $q_5 = 2.558$ rad, $q_6 = 0.756$ rad and $q_7 = 0.949$ rad. At the beginning of the simulation, LAR is located 0.08 m above the end-effector in the Z axis direction. It is assumed that orientations of the end-effector frame and the LAR frame coincide. Moreover, a stationary target is taken into account, so its velocities are set to zero. The desired position of the end-effector is defined to be 0.015 m above the LAR reference frame in the Z axis direction (gripper jaws need to be positioned above the LAR plane, so that grasping is possible). Furthermore, the initial velocities of the satellite-manipulator system are also equal to zero. The simulation lasts 17 s. Within the first 10 s, the desired trajectory of the end-effector in the LAR frame is given. After that time, constant position and orientation are considered as input signals of control algorithm. Such a solution is applied to stop the end-effector in the desired position and orientation as well as to reduce oscillations of the end-effector position and orientation in the final stage of motion.

The simplified contact model is taken into account to verify usefulness of the algorithms while external forces act on the manipulator. The contact model is based on the model presented by Uyama et al. (2012) and Pérez et al. (2018), but the damping part is omitted. It is assumed that external forces act on the end-effector only in the range of a sphere of radius equal to $r = 0.03$ m. Force value is proportional to the distance between the end-effector and the centre of the sphere, which is located in the constant position in the LAR frame: 0.015 m

below LAR in the Z axis direction. External forces expressed in the force/torque sensor reference frame are calculated according to the equation:

$$\mathbf{f}^{(FTS)} = \frac{k(r - \|\mathbf{p}_{EE}^{(F)}\|)}{r^3} \frac{\mathbf{p}_{EE}^{(F)}}{\|\mathbf{p}_{EE}^{(F)}\|},$$

(20)

where $k = 0.1$ N m^2, $\mathbf{p}_{EE}^{(F)}$ is the end-effector position with respect to the reference frame located in the centre of the force sphere and $\|\cdot\|$ denotes the Euclidean norm of a vector. No external torques are taken into account. Visualisation of the considered force sphere is presented in Figure 3. The centre of the force sphere is located in the point $(0,0,0)$, which is also the origin of the frame (F). Vectors on the graph correspond to the repulsive force acting on the manipulator and measured by the force/torque sensor at points located inside the sphere.
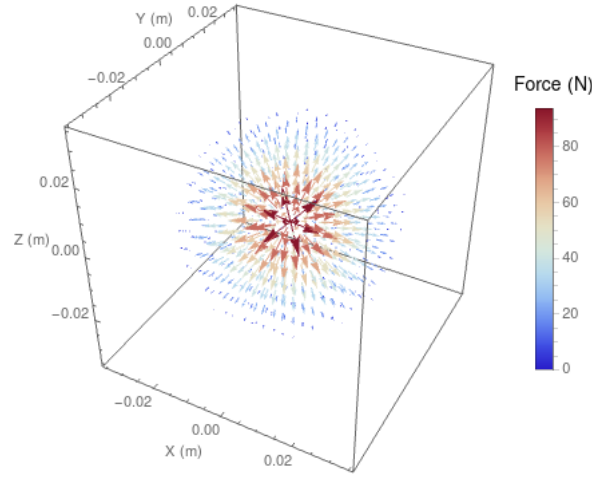

Figure 3. Visualisation of the force sphere

The presented active 6 DoF force/torque control algorithm was compared with the classical Cartesian control algorithm (Rybus et al., 2017) which allows to follow the desired trajectory but does not consider external forces acting on the end-effector. The control law for the Cartesian control algorithm is defined with the following equation:

$$\dot{\mathbf{q}}_{des} = \left(\mathbf{J}_{dyn}^{(EE)}\right)^{\#} \mathbf{K}\left(\left(\mathbf{P}_{POR}^{(LAR)}\right)_{des} - \mathbf{P}_{POR}^{(LAR)}\right),$$

(21)

where

$$\mathbf{K} = \begin{bmatrix} \mathbf{R}_{LAR}^{EE}\mathbf{K}_{lin} & \mathbf{0}_{3\times3} \\ \mathbf{0}_{3\times3} & \mathbf{R}_{LAR}^{EE}\mathbf{T}_{eul}\mathbf{K}_{eul} \end{bmatrix},$$

(22)

$\mathbf{K}_{lin}$ and $\mathbf{K}_{eul}$ are the Cartesian control gain matrices. To compare performance of the algorithms, the external forces generated by the contact model should have values of the same magnitude for both simulation cases. This goal may be achieved by the choice of high values of parameters for spring-mass-damper system modelled in the active 6 DoF force/torque control algorithm. Thus, the considered matrices are defined as $\mathbf{K}_d = diag_{6\times6}(600)$, $\mathbf{B}_d = diag_{6\times6}(500)$ and $\mathbf{M}_d = diag_{6\times6}(800)$. For Cartesian control algorithm, the gain matrices are chosen as $\mathbf{K}_{lin} = diag_{3\times3}(3)$ and $\mathbf{K}_{eul} = diag_{3\times3}(3)$. For both cases, joint torques are calculated based on joint angular velocities generated with the algorithm and joint angular velocities measured in the manipulator joints. These torques are generated using the Proportional-Integral-Derivative (PID) controllers, whose parameters are presented in Table 4. During the first second of the simulation, the parameters are scaled with a coefficient

dependent on time and equal to t^2 to avoid too rapid reaction of the control system and generation of very high joint torques.

Table 4. PID controllers gains

Joint	k_p	k_i	k_d
1	140	10	0.01
2	210	10	0.01
3	140	10	0.01
4	105	1	0.01
5	105	1	0.01
6	21	1	0.01
7	21	1	0.01

In the following figures, simulation results are presented. The results obtained for both control algorithms for the same simulation scenario are compared. Positions and orientations reached by the end-effector in the LAR frame are shown in Figure 4. Moreover, the desired trajectory is presented. Furthermore, Figure 5 shows the external forces generated using the adopted contact model. They had an influence on the momentum and angular momentum of the satellite-manipulator system; so, these values were also investigated. The momentum and angular momentum of the system are presented in Figure 6. Servicing satellite velocities are shown in Figure 7. Subsequently, measured joint torques for both control algorithms are shown in Figure 8. Analysis of the maximal absolute values of torques generated in each joint was conducted. These values are compared in Table 5. Finally, Figure 9 presents graphs of loads measured between the seventh link of the manipulator and the end-effector.
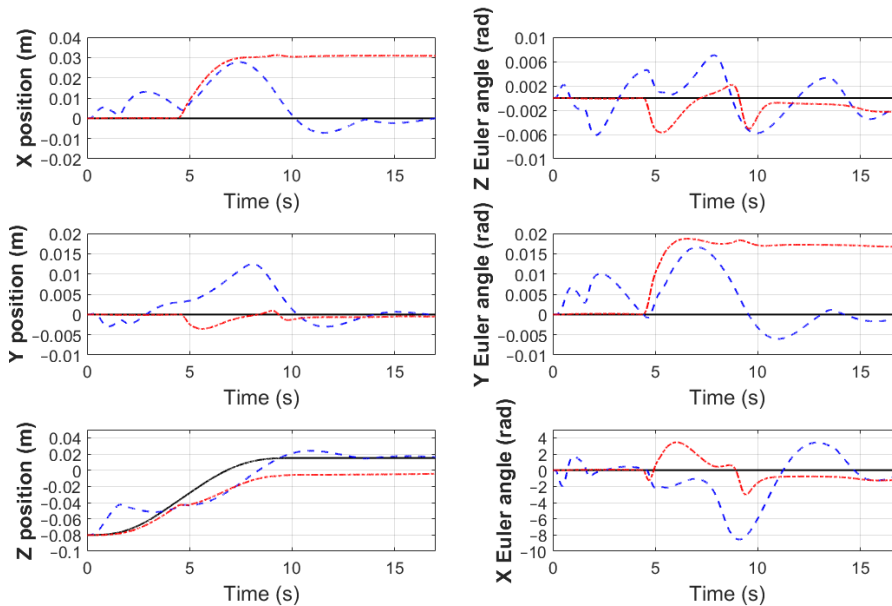

Figure 4. End-effector positions and orientations with respect to the LAR frame (blue dashed line – active 6 DoF force/torque control, red dotted line – Cartesian control, black solid line – desired)
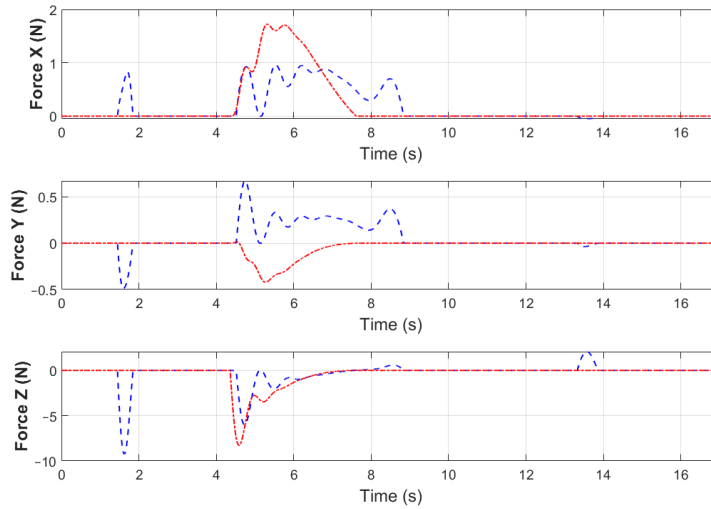
Figure 5. External forces from the contact model (blue dashed line – active 6 DoF force/torque control, red dotted line – Cartesian control)
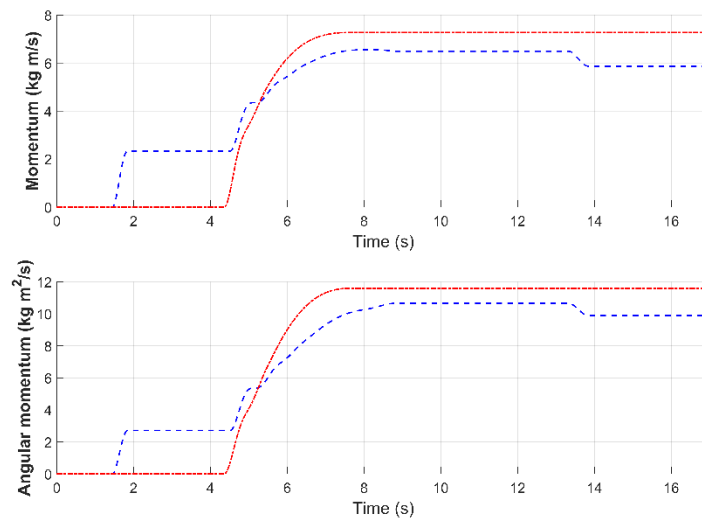

Figure 6. Resultant values of momentum and angular momentum of the satellite-manipulator system (blue dashed line – active 6 DoF force/torque control, red dotted line – Cartesian control)
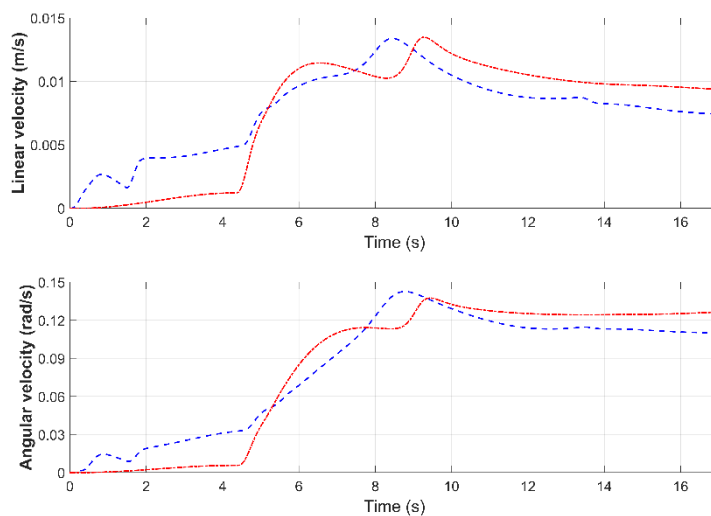

Figure 7. Resultant values of servicing satellite velocities (blue dashed line – active 6 DoF force/torque control, red dotted line – Cartesian control)
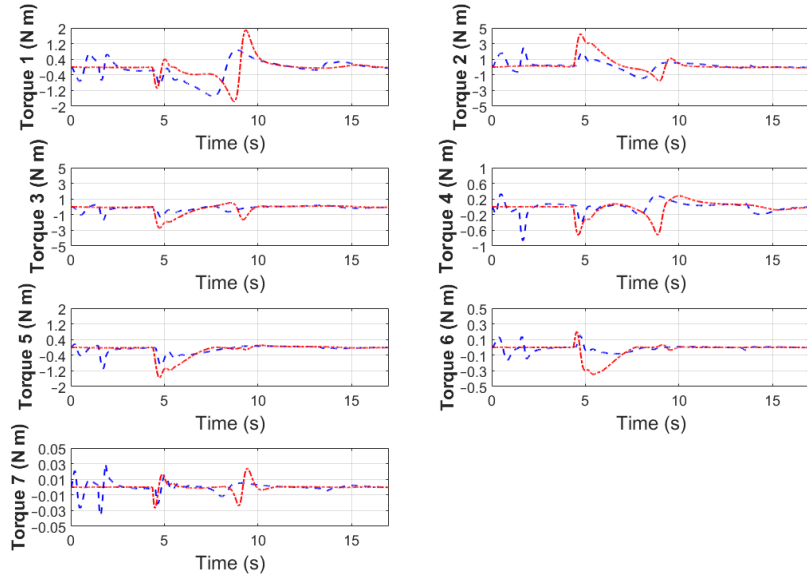
Figure 8. Measured joint torques (blue dashed line – active 6 DoF force/torque control, red dotted line – Cartesian control)
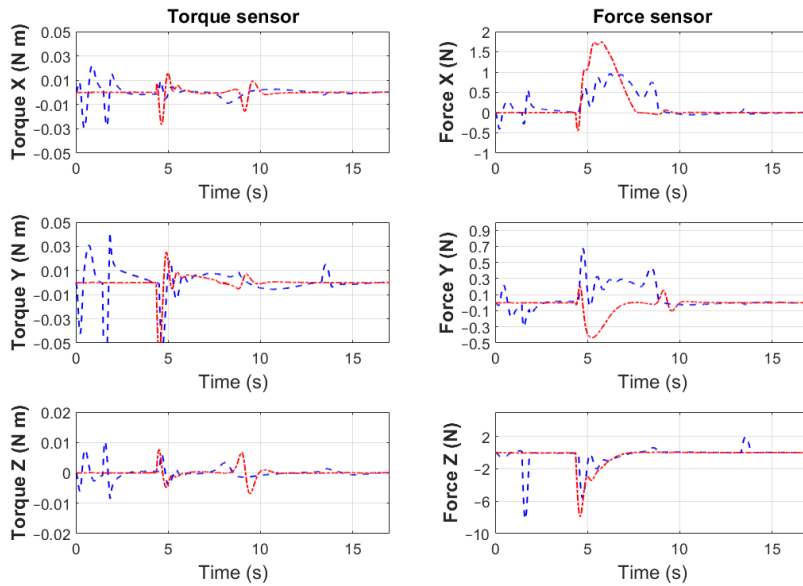

Figure 9. Loads measured between the seventh link and the end-effector (blue dashed line – active 6 DoF force/torque control, red dotted line – Cartesian control)

Table 5. Maximal values of measured joint torques

Joint	Active 6 DoF force/torque control (N m)	Cartesian control (N m)
1	1.50	1.89
2	2.45	4.21
3	1.68	2.72
4	0.86	0.72
5	1.10	1.55
6	0.17	0.35
7	0.036	0.027

5. DISCUSSION

The conducted simulations prove that the proposed active 6 DoF force/torque control allows to achieve better performance of the manipulator when external forces are applied to it compared with the Cartesian control. The usage of the admittance control algorithm allowed to reach the desired position and orientation more precisely, which can be seen in Figure 4. Although more oscillations around the defined trajectory may be observed, they gradually disappear. For the Cartesian control algorithm, constant and significant errors can be observed in some dimensions.

Due to different properties of control algorithms, in both considered simulation cases, the manipulator performed distinct motion. Thus, different external forces were generated. In particular, for the active 6 DoF force/torque control, the end-effector came into the range of the force sphere much earlier. It had a significant impact on momentum and angular momentum of the satellite-manipulator system. Application of external forces resulted in changes of these values. It was a significant difference compared to the assumption defined in Section 2 that the momentum and angular momentum are equal to zero. However, the active 6 DoF force/torque control algorithm allowed to compensate this disturbance quite well and reduced the maximum values of momentum and angular momentum. Uncompensated non-zero values of these parameters led to some inaccuracy in positioning of the end-effector, which can be particularly observed for the Cartesian control. Furthermore, a different behaviour of the manipulator in both cases is strictly connected with the servicing satellite velocities, which were higher for the Cartesian control. This aspect is also important as target may leave the manipulator workspace due to the motion of the manipulator base. Hence, the manoeuvre may not proceed successfully. High velocities of the servicing satellite may also result in the inability of the control system to compensate fast changes of the system position. The outer feedback loop for the position and orientation of the end-effector may be interpreted as a PID controller in case of the active 6 DoF force/torque control and as a P controller in case of the Cartesian control. Thus, reaction of the first considered algorithm is better.

The positioning of the end-effector in the LAR frame was better in case of the active 6 DoF force/torque control. In addition, the generated torques were lower. Comparison of the maximal absolute values in Table 5 shows that the usage of the Cartesian control resulted in higher joint torques in almost every joint. In particular, torque generated for joint 2 is almost 72 % higher when the Cartesian control is applied than for the admittance control. Even if some values generated with the active 6 DoF force/torque control are higher, the observed differences are not significant. It is worth noticing that lower joint torques were obtained despite the fact that the external forces were slightly higher and the end-effector was longer located in the range of the defined force sphere.

Finally, loads measured between the seventh link and the end-effector do not differ a lot for both algorithms. It may be also observed that values of forces generated in the contact model are similar. Such results were achieved due to the selection of high values of the coefficients of the gain matrices in the active 6 DoF force/torque control. However, decrease of the system stiffness, damping and inertia modelled for this control algorithm may result in higher external forces without loss of the quality of following the desired trajectory. In such an approach, the manipulator will be robust to higher external forces and simultaneously, it will compensate their influence better. On the other hand, higher joint torques may be generated. Selection of proper gains $\mathbf{K}_d$, $\mathbf{B}_d$ and $\mathbf{M}_d$ is important to reach the desired balance between following the desired trajectory and reaction to the external forces.

The discussed simulations were run using the MATLAB Simulink environment. Hence, to compare the computation time of every algorithm, time spent in executing each function was measured. For both cases, the most time-consuming process was calculating the pseudoinverse of the Dynamic Jacobian matrix. It took almost 70% of the computational time for the Cartesian control algorithm, while for the active 6 DoF force/torque control algorithm, it took almost 60% of the computational time. Other operations were not so time-consuming. However, the active 6 DoF force/torque algorithm requires more calculations. To compute the desired velocity of the end-effector, numerical derivatives and integrators are used. Moreover, angular velocities and accelerations are defined with some non-linear equations, which are based on Euler angles and their derivatives. Meanwhile, the classical Cartesian algorithm needs only to calculate angular velocities based on Euler angles once. Thus, it is clear that the proposed admittance control algorithm may be more time-consuming due to higher number of considered numerical operations, in particular, the non-linear ones. However, although the active 6 DoF force/torque algorithm is more complex, still the most difficult part of the algorithm is calculating the pseudoinverse of the Dynamic Jacobian matrix, which is common for both considered control algorithms. Thus, the observed differences should not be significant for the implementation of the proposed admittance control algorithm on the satellite on-board computer.

There are still a lot of possibilities to develop the presented approach. Further research on the active 6 DoF force/torque algorithm should consider more sophisticated contact model with a realistic architecture of the manipulator gripper. Moreover, experiments on real objects should be conducted, in particular, the ones in the conditions of microgravity. Such a study can be performed on a planar air-bearing microgravity simulator described by Basmadji et al. (2019) and Rybus et al. (2019). Alternatively, the algorithm may be verified with hardware-in-the loop tests using the KUBE platform (Granosik et al., 2016). It will be worthwhile especially due to the possibility of in-depth verification of the computational time measured in real application.

6. CONCLUSIONS

In this paper, the active 6 DoF force/torque control method for the manipulator mounted on the free-floating servicing satellite has been presented. The proposed approach is applicable for the grasping phase, in which the end-effector is approaching the selected grasping point on the non-cooperative target satellite. The main aim of the proposed method is to balance the relation between end-effector position and force along each direction in the Cartesian space. The 6 DoF force/torque control method was validated in numerical simulations with the simplified model of contact. The obtained results showed that the proposed solution allows to obtain better positioning of the end-effector and lower control torques in manipulator joints than the classical Cartesian control method. The presented approach can be applied in servicing and active debris removal missions.

REFERENCES

Almeida, F., Lopes, A., Abreu, P. (2000) Force-Impedance Control of Robotic Manipulators. *Proc. 4th Portuguese Conference on Automatic Control*, Guimarães, Portugal.

Basmadji, F.L., Rybus, T., Biedrzycka, A., Pawlus, M., Seweryn, K. (2018) Compliant control of the robotic arm during clamping operation in the e.Deorbit mission. *Proc. Clean Space Industrial Days*, ESTEC, Noordwijk, The Netherlands.

Basmadji, F.L., Chmaj, G., Rybus, T., Seweryn, K. (2019) Microgravity testbed for the development of space robot control systems and the demonstration of orbital maneuvers.

Proc. SPIE: Photonics Applications in Astronomy, Communications, Industry, and High-Energy Physics Experiments, Wilga, Poland.

Calanca, A., Muradore, R., Fiorini, P. (2016) A review of algorithms for compliant control of stiff and fixed-compliance robots. *IEEE/ASME Transactions on Mechatronics*, Vol. 21, No. 2, 613-624.

Cavenago, F., Giordano, A.M., Massari, M. (2019) Contact force observer for space robots. *Proc. 58th IEEE Conference on Decision and Control (CDC'2019)*, Nice, France.

Fehse, W. (2014) Rendezvous with and capture/removal of non-cooperative bodies in orbit: the technical challenges. *Journal of Space Safety Engineering*, Vol. 1, No. 1, 17-27.

García, J., Gonzalez, D., Rodríguez, A., Santamaria, B., Estremera, J., Armendia, M. (2019) Application of impedance control in robotic manipulators for spacecraft on-orbit servicing. *Proc. 24th IEEE International Conference on Emerging Technologies and Factory Automation (ETFA'2019)*, Zaragoza, Spain.

Granosik, G., Zubrycki, I., Soghbatyan, T., Zarychta, D., Gawryszewski, M. (2016) KUBE - platforma robotyczna dla badań naukowych i prac wdrożeniowych [in polish: KUBE - Robotic platform for research and implementation], *Prace Naukowe Politechniki Warszawskiej: Elektronika*, eds. Tchoń K., Zieliński C., Oficyna Wydawnicza Politechniki Warszawskiej, Warszawa, Vol. 195, No. 1, 223-234.

Henshaw, C.G., Glassner, S., Naasz, B., Roberts, B. (2022) Grappling Spacecraft. *Annual Review of Control, Robotics, and Autonomous Systems*, Vol. 5, 137-159, doi: 10.1146/annurev-control-042920-011106

Liu, X.F., Cai, G.P., Wang, M.M., Chen, W.J. (2020a) Contact control for grasping a non-cooperative satellite by a space robot. *Multibody System Dynamics*, Vol. 50, No. 2, 119-141.

Liu, X.F., Zhang, X.Y., Chen, P.C., Cai, G.P. (2020b) Hybrid control scheme for grasping a non-cooperative tumbling satellite. *IEEE Access*, Vol. 8, 54963-54978.

Luu, M.A., Hastings, D.E. (2021) Review of On-Orbit Servicing Considerations for Low-Earth Orbit Constellations. *Proc. ASCEND'2021 Conference*, Las Vegas, NV, USA.

Nakanishi, H., Yoshida, K. (2006) Impedance control for free-flying space robots-basic equations and applications. *Proc. IEEE/RSJ International Conference on Intelligent Robots and Systems 2006 (IROS'2006)*, Beijing, China.

Oleś, J., Rybus, T., Seweryn, K., Surowiec, M., Wojtyra, M., Pietras, M., Scheper, M. (2017) Testing and simulation of contact during on-orbit operations. *Proc. 14th Symposium on Advanced Space Technologies in Robotics and Automation (ASTRA'2017)*, Leiden, The Netherlands.

Palma, P., Seweryn, K., Rybus, T. (2022) Impedance Control Using Selected Compliant Prismatic Joint in a Free-Floating Space Manipulator, *Aerospace*, Vol. 9, No. 8, 406.

Pérez, P.R., De Stefano, M., Lampariello, R. (2018) Velocity matching compliant control for a space robot during capture of a free-floating target. *Proc. 2018 IEEE Aerospace Conference*, Big Sky, MT, USA.

Raibert, M.H., Craig, J.J. (1981) Hybrid position/force control of manipulators. *Journal of Dynamic Systems, Measurement, and Control*, Vol. 103, 126-133.

Ratajczak, J., Tchoń, K. (2020) Normal forms and singularities of non-holonomic robotic systems: a study of free-floating space robots. *Systems & Control Letters*, Vol. 138, 104661.

Rybus, T., Seweryn, K., Sąsiadek, J.Z. (2017) Control system for the free-floating space manipulator based on Nonlinear Model Predictive Control (NMPC). *Journal of Intelligent & Robotic Systems*, Vol. 85, No. 3, 491-509.

Rybus, T., Wojtunik, M., Basmadji, F.L. (2022) Optimal collision-free path planning of a free-floating space robot using spline-based trajectories. *Acta Astronautica*, Vol. 190, 395-408.

Rybus, T., Lisowski, J., Seweryn, K., Barciński, T. (2012) Numerical Simulations and Analytical Analysis of the Orbital Capture Maneouvre as a Part of the Manipulator-Equipped Servicing Satellite Design. *Proc. 17th International Conference on Methods and Models in Automation and Control (MMAR'2012)*, Międzyzdroje, Poland.

Rybus, T., Seweryn, K., Oleś, J., Basmadji, F.L., Tarenko, K., Moczydłowski, R., Barciński, T., Kindracki, J., Mężyk, Ł., Paszkiewicz, P., Wolański, P. (2019) Application of a planar air-bearing microgravity simulator for demonstration of operations required for an orbital capture with a manipulator. *Acta Astronautica,* Vol. 155, 211–229.

Seweryn, K., Banaszkiewicz, M. (2008) Optimization of the trajectory of a general free-flying manipulator during the rendezvous maneuver. *Proc. AIAA Guidance, Navigation, and Control Conference and Exhibit (AIAA-GNC'2008)*, Honolulu, HI, USA.

Shan, M., Guo, J., Gill, E. (2016) Review and comparison of active space debris capturing and removal methods. *Progress in Aerospace Sciences*, Vol. 80, 18-32.

Tasker, F., Henshaw, C. (2008) Managing contact dynamics for orbital robotic servicing missions. *Proc. AIAA SPACE 2008 Conference & Exposition (AIAA SPACE'2008)*, San Diego, CA, USA.

Uyama, N., Nakanishi, H., Nagaoka, K., Yoshida, K. (2012) Impedance-based contact control of a free-flying space robot with a compliant wrist for non-cooperative satellite capture. *Proc. IEEE/RSJ International Conference on Intelligent Robots and Systems 2012 (IROS'2012)*, Vilamoura-Algarve, Portugal.

Villani, L., De Schutter, J. (2016) Force control, *Springer handbook of robotics*, eds. Siciliano, B., Khatib, O., Springer, Cham, 195-220.

Wang, J., Li, Y. (2010) Hybrid impedance control of a 3-DOF robotic arm used for rehabilitation treatment. *Proc. IEEE International Conference on Automation Science and Engineering 2010 (CASE'2010)*, Toronto, Canada.

Wilde, M., Kwok Choon, S., Grompone, A., Romano, M. (2018) Equations of Motion of Free-Floating Spacecraft-Manipulator Systems: An Engineer's Tutorial, *Frontiers in Robotics and AI*, Vol. 5, No. 41, doi: 10.3389/frobt.2018.00041.

Wu, S., Mou, F., Ma, O. (2017) Contact dynamics and control of a space manipulator capturing a rotating object. *Proc. AIAA Guidance, Navigation, and Control Conference (AIAA GNC'2017)*, Grapevine, TX, USA.